

# Learning material synthesis-structure-property relationship by data fusion: Bayesian Coregionalization N-Dimensional Piecewise Function Learning

A. Gilad Kusne<sup>1,2</sup> (ORCID: 0000-0001-8904-2087), Austin McDannald<sup>1</sup> (ORCID: 0000-0002-3767-926X),  
Brian DeCost<sup>1</sup> (ORCID: 0000-0002-3459-5888)

1. Materials Measurement Science Division, Material Measurement Laboratory, National Institute of Standards and Technology, Gaithersburg MD

2. Materials Science & Engineering Dept, University of Maryland, College Park MD

## Abstract:

Advanced materials are needed to further next-generation technologies such as quantum computing, carbon capture, and low-cost medical imaging. However, advanced materials discovery is confounded by two fundamental challenges: the challenge of a high-dimensional, complex materials search space and the challenge of combining knowledge, i.e., data fusion across instruments and labs. To overcome the first challenge, researchers employ knowledge of the underlying material synthesis-structure-property relationship, as a material's structure is often predictive of its functional property and vice versa. For example, optimal materials often occur along composition-phase boundaries or within specific phase regions. Additionally, knowledge of the synthesis-structure-property relationship is fundamental to understanding underlying physical mechanisms. However, quantifying the synthesis-structure-property relationship requires overcoming the second challenge. Researchers must merge knowledge gathered across instruments, measurement modalities, and even laboratories. We present the Synthesis-structure-property relationship coreGionalized IEArner (SAGE) algorithm. A fully Bayesian algorithm that uses multimodal coregionalization to merge knowledge across data sources to learn synthesis-structure-property relationships.

## Introduction:

A lack of advanced materials stymies many next-generation technologies such as quantum computing, carbon capture, and low-cost medical imaging. However, fundamental challenges stand in the way of discovering novel and optimized materials including 1) the challenge of a high-dimensional, complex materials search space and 2) the challenge of integrating knowledge across instruments and labs, i.e., data fusion. The first challenge arises from the need to explore ever-more complex materials as simpler material systems are exhausted. Here material system refers to the materials resulting from a set of material synthesis or processing conditions. With each new material synthesis condition, the number of potential experiments grows exponentially – rapidly escape the feasibility of Edisonian-type studies, forming a high-dimensional search space. As a result, any data is typically sparse relative to the search space. The search space is also highly complex due to the underlying complex relationship between material synthesis conditions and the resulting material structure and functional properties, i.e., the material synthesis-structure-property relationship (SSPR).

Researchers use knowledge of the SSPR as a blueprint to navigate the high-dimensional complex search space toward novel and optimized materials. Building the SSPR blueprint involves combining knowledge of material synthesis conditions, lattice structure (and potentially microstructure), as well as the diverse set of functional properties required to meet the technological requirements. This requires integrating data across different instruments and measurement modalities, each dependent on differing physical

principles. Additionally, measurements can vary based on instrument calibration, measurement parameter settings, environmental conditions such as temperature and humidity, and each instrument user's measurement process. Even instruments of the same make and model differ based on unique biases, uncertainties, and data artifacts.

As a very common example, researchers often start their search for improved materials with the phase map of the target material system. A phase map (or 'phase diagram' for equilibrium materials) visualizes the synthesis-structure relationship. An example phase map is shown in Figure 1a for the  $(\text{Bi},\text{Sm})(\text{Sc},\text{Fe})\text{O}_3$  material system (1). Here the phase map relates material composition (the target synthesis conditions) to resulting lattice structure, described in terms of phases, *i.e.*, composition-structure prototypes. The phase map is divided into phase regions – contiguous regions of synthesis space (experiments of varying synthesis conditions) that result in materials of the same set of phases. The regions are separated by phase boundaries (dashed black lines). Material phase information is predictive of many functional properties. Materials with property extrema tend to occur either within specific phase regions (*e.g.*, magnetism and superconductivity) or along phase boundaries (*e.g.*, caloric-cooling materials). Thus, a materials researcher can use phase maps to guide their studies toward synthesis conditions that are expected to produce materials with more promising properties.

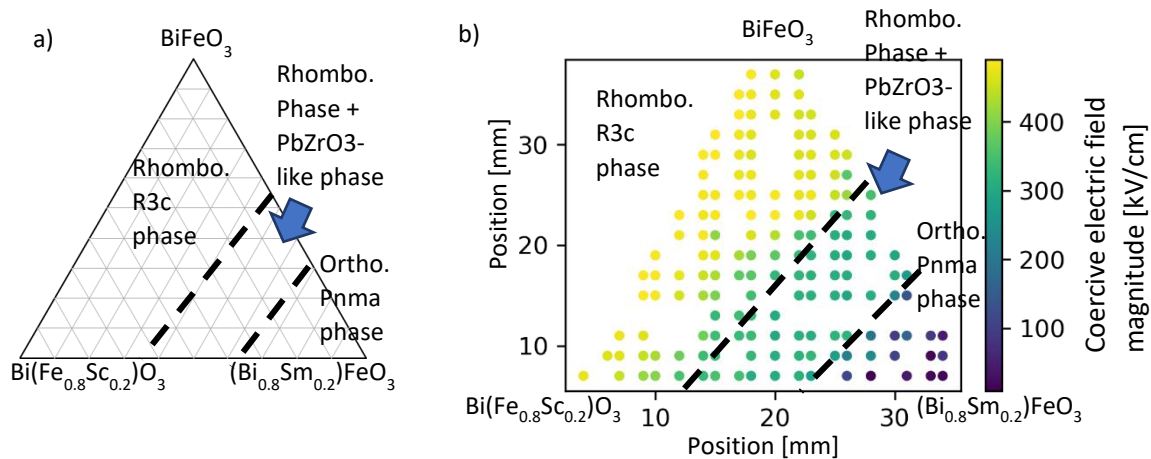


Figure 1. The  $(\text{Bi},\text{Sm})(\text{Sc},\text{Fe})\text{O}_3$  material system. a) Experimentally identified phase diagram. Phase boundaries indicated by black dashed lines. b) Coercive electric field magnitude overlaid with phase diagram. Circles indicate experimentally characterized materials and color indicates coercive electric field magnitude between 0 kV/cm and 491 kV/cm.

Figure 1b visualizes a  $(\text{Bi},\text{Sm})(\text{Sc},\text{Fe})\text{O}_3$  SSPR by combining the phase map with the functional property of coercive electric field magnitude (CEFM) (2, 3). Circles indicate experimentally characterized materials and circle color indicates measured CEFM. The CEFM is highly dependent on both synthesis conditions and phase, with the highest values occurring with 'open' hysteresis loops in the rhombohedral R3c phase region. Additionally, the composition dependence of CEFM significantly differs between phase regions, with greater variation occurring in the R3c and Pnma phase regions than the intermediary region. In general, discontinuities in functional property values may also occur at phase boundaries. Thus, functional properties can be represented as piecewise functions of the synthesis parameters (in this case composition), with each 'piece' of the piecewise function associated with a phase region. This allows for

significant changes in function behavior from region to region and/or discontinuities to occur at phase boundaries.

To overcome the dual challenges of a complex, high-dimensional search space and data fusion in SSPR learning, we present the Synthesis-structure-property relAtionship coreGionalized lEArner (SAGE). SAGE is a Bayesian machine learning (ML) algorithm that combines three features: 1) ML-based segmentation of the synthesis space using material synthesis and phase data. Segments are phase regions, and the collection of phase regions forms the synthesis-phase map. The synthesis-phase map is then used to extrapolate the synthesis-structure relationship to new materials, 2) piecewise regression to fit and extrapolate synthesis-property relationships, and 3) coregionalization. Coregionalization allows multimodal, disparate knowledge of structure (1) and property (2), both gathered across the shared domain of synthesis conditions, to be combined to exploit shared trends. SAGE combines these three features to learn the most likely SSPR given material synthesis, structure, and property data. Additionally, SAGE's Bayesian framework allows for full uncertainty quantification and propagation. A schematic of SAGE is provided in Figure 2.

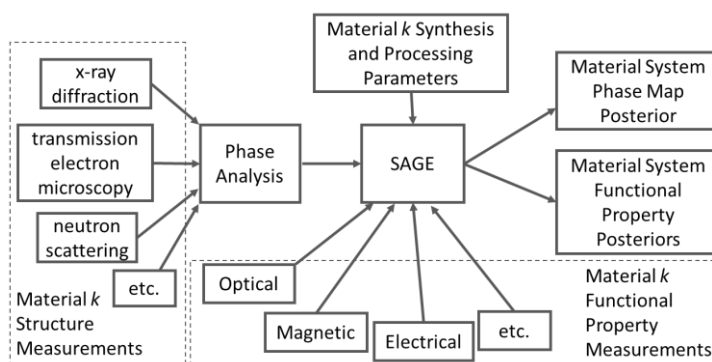


Figure 2. SAGE Schematic. A collection of materials spanning a target material system are characterized for multimodal structure data which is then processed through a preliminary phase analysis tool. The materials are also characterized for a range of functional properties. The collected data is passed to SAGE which outputs posterior probabilities for both the material system phase map and the functional properties.

Each of SAGE's features has a diverse history. The first feature of ML-based phase mapping has a seen the development of an array of algorithms over the last few decades (3–7). These algorithms combine two tasks, 1) data analysis: analyzing structure data to identify phase abundances or phase regions and 2) extrapolation: extrapolating phase knowledge from measured materials to unmeasured materials. Data analysis techniques include matrix factorization, peak detection, graphical model segmentation, constraint programming, mixed integer programming, and deep learning, among others (3, 8–16). Extrapolation algorithms have focused primarily on the use of graph-based models or Gaussian processes (GP) (9, 10, 17, 18). For the present work, we assume the task of structure data analysis is addressed with one of the many available algorithms. SAGE therefore begins with knowledge of phase and focuses on the task of extrapolating phase map knowledge through Bayesian coregionalized synthesis space segmentation.

Piecewise function regression algorithms have a much longer history. This includes the common challenge of detecting data discontinuities - also known as jumps or changepoints, which can be generalized to

higher dimensions as edges (19), change-boundaries, and change-surfaces. Change-point detection algorithms are quite diverse, using function derivatives, filter convolution, Bayesian inference, and more recently, adaptive design (20). Common methods for piecewise regression include linear piecewise algorithms and splines. We point the reader to review articles in these fields (21, 22). Specifically for GPs, multiple piecewise modeling methods exist (23) including the use of the changepoint kernel (24). This includes recent work which assumes that the target data is the sum of random processes and then seeks to identify the constituent processes by jointly solving a GP regression fit with a Bayesian inference model fit, where the model may include changepoint detection (25). This latter method may suffer when correlations exist between the constituent processes or when the assumed model for the Bayesian inference fit is overly flexible, capturing information from one of the other constituent processes. As such, this method may result in incorrect predictions and uncertainty quantification.

The field of coregionalization developed from geospatial science to learn functions with shared trends over the same physical domain (26, 27). Data for each target function is not required to be collected for the same set of points in the input domain (27). For example, if one seeks to learn  $f_1: x \rightarrow y$  and  $f_2: x \rightarrow s$ , data  $D_1 = \{(x_k, y_k)\}_{k=1}^N$  and  $D_2 = \{(x_l, s_l)\}_{l=1}^M$ , the set of input locations  $\{x_k\}_{k=1}^N$  and  $\{x_l\}_{l=1}^M$  are not required to correspond to the same locations. Alternative methods for jointly learning related functions include multi-task learning, co-kriging, including multi-task Gaussian processes (28, 29) as well as constraint programming methods and Bayesian methods (27, 30, 31). These algorithms focus on exploiting similarities between functions over the full underlying shared domain, assume the set of output functions are similar (*e.g.*, all continuous), and assume that each experiment is characterized similarly. Recent work tackles learning heterogeneous sets of functions such as a mix of continuous, categorical, and binary outputs (32). These algorithms assume a correlation between a set of latent functions that contribute to the observed output functions.

Our challenge is unique. While we seek to jointly learn the synthesis-structure relationship and synthesis-property relationships, the correlation of interest between these relationships is purely that of discontinuities, rather than correlations over the full synthesis domain. We assume that phase boundaries indicate potential change surfaces in functional properties, and vice versa. We wish to jointly learn these phase boundaries and utilize them to define piecewise functions for the functional properties, allowing for different property behavior in different phase regions. Prior algorithms fail for this challenge as the synthesis-structure relationship and those of synthesis-properties are not correlated over the full synthesis domain (this is also true for latent function representations). Additionally, SAGE utilizes coregionalization to allow different measurements to be performed at different locations in the shared synthesis domain. This is commonly the case when materials synthesis experiments take equal or less time than the measurements or when combining data collected at different times or by different labs.

To the authors' knowledge, the only algorithm that addresses the same challenge is the closed-loop autonomous materials exploration and optimization (CAMEO) algorithm (9). CAMEO first learns phase boundaries from synthesis and structure data and then utilizes this knowledge to define the change boundaries in the piecewise function used to fit and model functional property data. This two-step approach was employed in driving an x-ray diffraction-based autonomous (robot) materials research system in the study of phase-change memory material. The study resulted in the discovery of the current best-in-class phase-change memory material – the first autonomous discovery of a best-in-class solid state material (9). SAGE improves on CAMEO by allowing full Bayesian uncertainty quantification and

propagation. SAGE also jointly solves for the SSPR to better exploit shared trends across structure and property data and improve SSPR knowledge. SAGE is offered as a module of CAMEO, *i.e.*, CAMEO-SAGE.

The present data science challenge is generalizable beyond learning SSPR. One can use SAGE to address the more common issue of having successful and failed experiments across a shared experiment parameter domain. SAGE would then learn and exploit knowledge of the success-failure boundary to improve prediction of properties of either type of experiments. Additionally, SAGE addresses data fusion across instruments, measurement modalities and labs. The common approach to this data fusion challenge is to map data from different sources into the same data space, allowing comparison. For example, data fusion for x-ray diffraction measurements requires removing source-based data artifacts including instrument effects that are convolved into the data. That data must then also be mapped from the source-based independent variable space ( $2\theta$ ) to an instrument-free independent variable space ( $q$ ). In general, data mapping to an instrument (also lab, weather, etc.) invariant space requires a significant amount of meta data that is often not available.

An alternative is to independently analyze the data from each source and then combine the derived knowledge across sources. SAGE allows such limited-metadata data fusion. For example, for structure data, one performs phase mapping analysis for each data source and then SAGE coregionalization combines knowledge across sources. A similar benefit exists for functional property data by treating data from each source as a different target property, *e.g.*, `coercivity_data_source_1` and `coercivity_data_source_2`. Additionally, SAGE may be applied to cases where only structure data or only functional property data is obtained.

The contributions of this work are:

- 1-dimensional and N-dimensional Bayesian algorithms for coregionalized joint segmentation and piecewise regression.
- Associated constraint programming algorithms for coregionalized joint segmentation and piecewise regression.
- Demonstration of Bayesian algorithms for SSPR learning.

## Algorithms

We present coregionalization algorithms for combining multiple data sources for materials synthesis, structure, and property to learn the SSPR over the shared synthesis domain  $\mathbf{x} \in \mathbf{X}$ . Structure data from data source  $i$  is represented by  $D_{s,i} = \{\mathbf{x}_k, \mathbf{z}_{k,i}\}_{k=1}^{N_i}$  for material  $\mathbf{x}_k$  (data pair indexed with  $k$ ) and its associated structure descriptor  $\mathbf{z}_{k,i}$ , with  $N_i$  data pairs collected from data source  $i$ . The full set of structure data is labeled  $D_s$ , where the subscript  $s$  indicated structure-associated data. Similarly, property data from data source  $j$  is represented by  $D_{p,j} = \{\mathbf{x}_l, \mathbf{y}_{l,j}\}_{l=1}^{N_j}$  for material  $\mathbf{x}_l$  and its associated material property measurement  $\mathbf{y}_{l,j}$ , and where subscript  $p$  indicates functional-property-associated data.  $D_{s,i,k}$  and  $D_{p,j,k}$  are the  $i$ -sourced structure data for  $\mathbf{x}_k$  and the  $j$ -sourced functional property data for  $\mathbf{x}_l$ . For this work we assume each data source provides data for one property. The full set of functional property data is labeled  $D_p$ . This representation allows for duplicate measurements of the same material from different data sources.

## Constraint Programming

The constraint programming algorithm (Eqn. 1) is defined by finding the set of parameters  $\theta = \{\theta_s, \theta_p\}$  that minimize the objective function  $Obj$ . The phase map is described by the function  $f_s(\mathbf{x}, \theta_s)$  which maps each point  $\mathbf{x}$  in the target synthesis space  $\mathbf{X}$  to a set of phase labels  $\mathbf{s}$ ,  $f_s: \mathbf{x} \rightarrow \mathbf{s}$ , where  $\theta_s$  is the associated set of parameters. The functional property is described by the piecewise function  $f_p(\mathbf{x}, f_s, \theta_p)$  which maps each point  $\mathbf{x}$  to a set of functional properties  $\mathbf{y}$ , *i.e.*,  $f_p: \mathbf{x} \rightarrow \mathbf{y}$ . This function is dependent on the set of parameters  $\theta_p$  and its piecewise nature is dependent on  $f_s$ . The functions  $d_s$  and  $d_p$  compute the relationship – typically the loss, between the function  $f_s$  and data  $D_s$  or between  $f_p$  and data  $D_p$ , respectively. For example,  $d_p$  can combine a measure of goodness of fit of  $f_p$  and model complexity, *e.g.*, the Bayesian information criteria (33). To quantify loss for structure data, the data  $D_s$  must also be mapped to a set of phase map labels, here performed by the function  $m_s(D_s)$  (As discussed above, this function is one of the many found in the literature). Minimizing the objective involves: 1) identifying potential values for parameters  $\theta_s$ , 2) solving for  $m_s(D_s)$  and  $f_s$ , 3) identifying potential values for parameters  $\theta_p$ , 4) solving for  $f_p$ , and 5) computing the overall loss for the objective function. This iterative approach allows a target property estimate to inform the subsequent optimization of  $f_s(\mathbf{x})$ .

$$Obj = \min_{\{\theta_s, \theta_p\}} [d_s(f_s(\mathbf{x}, \theta_s), m_s(D_s)) + d_p(f_p(\mathbf{x}, f_s, \theta_p), D_p)], \quad \text{Eqn. 1}$$

If the loss functions are additive across datasets, we have:

$$Obj = \min_{\{\theta_s, \theta_p\}} \left[ \sum_i d_s(f_s(\mathbf{x}, \theta_s), m_s(D_{s,i})) + \sum_j d_p(f_p(\mathbf{x}, f_s, \theta_p), D_{p,j}) \right], \quad \text{Eqn. 2}$$

One implementation has  $f_s$  map each point to an integer label associated with a given phase region. The function  $m_s$  is then required to map the structure data to potential phase region labels similar to those of (3–8). Alternatively, one may want the overall algorithm to identify phase abundances for each material  $\mathbf{x}$ . For this case,  $m_s$  identifies phase abundances and maps  $\mathbf{x}$  to phase region labels. Abundance regression can then be performed by including abundances in the list of target properties  $\mathbf{y}_p$ .

The Bayesian model presented below can be solved using such an objective function. Here,  $d_s$  and  $d_p$  are the negative log likelihood functions  $d_s = -\ln[p(f_s(\mathbf{x}, \theta_s)|m_s(D_s))]$  and  $d_p = -\ln[p(d_p(f_p(\mathbf{x}, f_s, \theta_p)|D_{p,j}))]$ , *i.e.*, the negative log likelihood of data  $\{D_s, D_p\}$  being observed for functions  $\{f_s, f_p\}$ . The notation  $p$  represents a pdf,  $p(a|b)$  describes the pdf of  $a$  given  $b$ , and for the equations below,  $a \sim p(b)$  indicates drawing independent and identically distributed samples from  $p(b)$ . Solving for  $\{\theta_s, \theta_p\}$  may be done under the variational inference approximation. The results presented her focus on Markov Chain Monte Carlo (MCMC) computed posteriors. The variational inference approximation can be used to initialize MCMC and speed up calculations.

## Bayesian Models

We provide two Bayesian models, one for challenges where  $\mathbf{X}$  is one dimensional (*i.e.*, only one synthesis parameter is investigated) and one where  $\mathbf{X}$  is of arbitrary dimension. Rather than minimizing loss, the aim of these models is to maximize the sum log likelihood  $L$  over the set of parameters and observed data (*e.g.*, minimize sum of negative log likelihood as above). Here, MCMC is used to compute

a posterior for each model parameter. Additionally, one can incorporate prior physical knowledge by modifying parameter prior probability density functions (pdf). Both models output an estimate for the posterior of the SSPR and each parameter (given the model and data) – providing both an estimate and uncertainty, compared to the constraint programming algorithm which outputs a point estimate (estimates of the uncertainty can also be obtained). The posteriors can be used in further Bayesian analysis as demonstrated below. The MCMC Bayesian inference method for evaluating the models consists of: 1) sampling function parameters, 2) using the samples to define  $f_s$  and  $f_p$ , and then 3) compute the log likelihood  $L$ .

Model 1 provides the general model. One first samples the function parameter priors for  $\theta_s$  and  $\theta_p = \{\theta_{p,j,r}\}$  for each  $j$  of  $J$  functional properties (or function property data source) and each  $r$  of  $R$  phase regions.  $f_{p,j}$  is a piecewise random process with different behavior  $f_{p,j,r}$  for each functional property in each phase region, i.e., different kernel hyperparameters for each phase region.  $f_s$  is used to compute the categorical distribution  $p(r(x))$  of phase regions labels for each point  $x$ .  $p(r(x))$  is used to compute the sum log likelihood  $L_s$  of structure data observations and identify phase region label probabilities for each functional property observation data point  $x_p$ . The sum log likelihood of the observed functional properties  $L_p$  is computed using these probabilities and the piecewise  $f_{p,j}$ . The total likelihood  $L$  is then returned, guiding Bayesian inference sampling. The implementations and associated code work with an arbitrary number of data sources. Sampling from GPs uses the Cholesky decomposition method to improve MCMC stability (34).

#### Model 1: General SAGE Model

- 1  $\theta_s \sim \text{prior}_{\theta_s}$
- 2  $\theta_p = \{\theta_{p,j,r}\}_{j=1, r=1}^{j=J, r=R} \sim \text{prior}_{\theta_{p,j,r}}$
- 3  $p_r(r) = p_r(r(x) = l) = \text{Categorical}(f_s(\theta_s))$
- 4  $L_s = \sum_i \sum_k \ln [p(m(D_{s,i,k}) | p_r(r))]$
- 5  $f_{p,j} = \sum_r f_{p,j,r}(\theta_{p,j,r}) p_r(r)$
- 6  $L_p = \sum_j \sum_k \ln [p(D_{p,j,k} | N(f_{p,j}, \theta_p))]$
- 7  $L = L_s + L_p$

After Bayesian inference is run, i.e., each  $b$  sample of  $B$  total MCMC samples are collected, the Bayesian posteriors for the phase map and functional-properties-describing functions are approximated. Here the categorical distribution describing the phase map is computed by taking  $\text{mean}_b[p_b(r)]$ , the posterior mean over the sampled categorical distributions. The phase map estimate  $\hat{p}$  and uncertainty  $e_{\hat{p}}$  are then computed with  $\hat{p} = \text{argmax}_r[p_M]$  and  $e_{\hat{p}} = \text{entropy}_r[p_M]$ . Each functional property is described by the posterior multivariate normal distribution  $N(\text{mean}_b[f_{p,j,b}], \text{std}_b[f_{p,j,b}])$  with additional measurement noise  $\text{mean}_b[n_{p,j,b}]$ .

#### Post MCMC Bayesian analysis.

For the Bayesian inference sample index  $b$ :

- 1  $p_M = \text{mean}_b[p_b(r)]$
- 2  $\hat{p} = \text{argmax}_r[p_M]$

```

3   $e_{\hat{p}} = \text{entropy}_r[p_M]$ 
4   $\hat{\mu}_{p,j} = \text{mean}_b[f_{p,j,b}]$ 
5   $\hat{\sigma}_{p,j} = \text{standard\_deviation}_b[f_{p,j,b}]$ 
6   $\hat{n}_{p,j} = \text{mean}_b[n_{p,j,b}]$ 
7   $\hat{f}_{p,j} = N(\hat{\mu}_{p,j}, \hat{\sigma}_{p,j})$ 
8   $\hat{y}_{p,j} = N(\hat{\mu}_{p,j}, \hat{\sigma}_{p,j} + \hat{n}_{p,j})$ 

```

### One Dimensional Challenges

When  $\mathbf{X}$  is one dimensional, phase boundaries may be represented as change points. The set of structure model parameters  $\theta_s$  are simply a set of changepoints in  $\mathbf{X}$ . The changepoints  $\theta_s$  are sampled and then converted to categorical distribution  $p(r) = f_s(x)$ . Each continuous region of  $\mathbf{X}$ , bounded by either a change point or the edge of the search space, defines a phase region  $r$ . For example, for a 2-phase region challenge over  $\mathbf{X} = [0, 1]$  with one changepoint at arbitrary value 0.5, phase region 0 would have a probability of 1 at  $x \leq 0.5$  and a probability of 0 for  $x > 0.5$  and vice versa for phase region 1. The categorical distribution is then used to compute the likelihood of the observations given the samples.

The presented implementation is developed from that of (18). The functional property in each phase region is represented by an independent radial basis function kernel Gaussian process, with  $\theta_p$  including:  $l_{r,j}$  kernel length scale,  $s_{r,j}$  kernel standard deviation (also known as ‘scale’), and  $s_j$  measured noise standard deviation. For this work, we assume that  $s_j$  is the same for property  $j$  across all phase regions. For each property, the region-specific functions  $f_{p,j,r}$  are sampled from  $GP(\theta_{p,j,r})$  and then combined using the probabilistic weights  $p(r)$  to give the piecewise functions  $f_{p,j}$ .  $f_{p,j}$  describes the sample mean and  $n_j$  the sample noise of the multivariate distribution  $N(f_{p,j}, n_j)$  used to describe a potential generating random process. Data likelihood is then given by  $p(D_{p,j} | N(f_{p,j}, n_j))$ .

Example Implementation:

#### Model 2: 1-Dimensional SAGE

```

1   $\theta_s \sim \text{Uniform}(\mathbf{X})$ 
2   $l_{r,j} \sim \text{Uniform}(\text{min\_length\_scale}_{r,j}, \text{max\_length\_scale}_{r,j})$ 
3   $s_{r,j} \sim \text{Uniform}(\text{min\_standard\_deviation}_{r,j}, \text{max\_standard\_deviation}_{r,j})$ 
4   $n_j \sim \text{Uniform}(\text{min\_noise\_scale}_j, \text{max\_noise\_scale}_j)$ 
5   $\mathbf{M}_s = \text{membership}(\theta_s, \mathbf{x}_s)$ 
6   $p_r(r) = p_r(r(\mathbf{x}) = l) = \text{Categorical}(\theta_s)$ 
7   $L_s = \sum_i \sum_k \ln [p(m(D_{s,i}) | p_r(r))]$ 
8   $f_{p,j,r} \sim GP_{j,r}(l_{r,j}, s_{r,j}, n_j)$ 
9   $f_{p,j} = \sum_r f_{p,j,r} p(r)$ 
10  $L_p = \sum_j \sum_r \ln [p(D_{p,j} | N(f_{p,j}, n_j))]$ 
11  $L = L_s + L_p$ 

```



## N Dimensional Challenges

Change boundaries and surfaces are not easy to define in higher dimensions, so we instead sample latent functions  $w(\mathbf{x})$  and then translate these latent functions into categorical distributions for phase region labels over  $\mathbf{X}$ . We define an N-dimensional multivariate normal distribution for the latent functions with associated parameters  $\theta_s$ . For an SSPR with R phase regions, we take R latent function samples, again, using the Cholesky decomposition method. The samples  $w(\mathbf{x})$  are then used to define the columns of matrix  $\mathbf{M}_s$ , i.e.,  $\mathbf{M}_s[:, r] = w_r$ . Each entry of  $\mathbf{M}_s[k, r]$  is taken as the unnormalized event log probability (and converted to logits by the Categorical distribution function) for point  $\mathbf{x}_k$  belonging to phase region label  $r$ . Here, each functional property is described by a N-dimensional GP.

### Model 3: N-Dimensional SAGE

```

1       $\mathbf{l}_s \sim ND\_Uniform(\min\_length\_scale_s, \max\_length\_scale_s)$ 
2       $\mathbf{s}_s \sim ND\_Uniform(\min\_standard\_deviation_s, \max\_standard\_deviation_s)$ 
3       $\theta_s = \{\mathbf{l}_s, \mathbf{s}_s\}$ 
4       $\mathbf{W}_k(\mathbf{x}) = \{w_h(\mathbf{x})\}_{h=1}^R \sim N(0, K_{Matern\ 5/2}(\mathbf{x}, \mathbf{x}', \theta_s))$ 
5       $p(r) = p(r(\mathbf{x}) = l) = \exp w_{r=l}(\mathbf{x}) / \sum_r \exp w_r(\mathbf{x})$ 
6       $L_s = \sum_i \sum_k \ln [p(m(D_{s,i})|p(r))]$ 
7       $\mathbf{l}_{r,j} \sim ND\_Uniform(\min\_length\_scale_{r,j}, \max\_length\_scale_{r,j})$ 
8       $\mathbf{s}_{r,j} \sim ND\_Uniform(\min\_standard\_deviation_{r,j}, \max\_standard\_deviation_{r,j})$ 
9       $n_j \sim Uniform(\min\_noise\_scale_j, \max\_noise\_scale_j)$ 
10      $b_{j,r} \sim Uniform(\min\_bias_{r,j}, \max\_bias_{r,j})$ 
11      $f_{p,j,r} \sim N(b_{j,r}, K_{RBF}(\mathbf{x}, \mathbf{x}', \mathbf{l}_{r,j}, \mathbf{s}_{r,j}, n_j))$ 
12      $f_{p,j} = \sum_r f_{p,j,r} p(r)$ 
13      $L_p = \sum_j \sum_r \ln [p(D_{p,j} | N(f_{p,j}, n_j))]$ 
14      $L = L_s + L_p$ 

```

## Additional Algorithms

In this work, we compare SAGE to off the shelf GP algorithms and modified versions of SAGE. We compare SAGE's phase mapping (PM) performance with a version of SAGE which only takes structure data input. For 1D challenges this is Model 4 'SAGE-1D-PM' and for 2D challenges this is Model 6 'SAGE-ND-PM'. We compare SAGE's functional property (FP) prediction performance with versions that only take in functional property data, i.e., piecewise Gaussian process regression. For 1D challenges this is Model 5 'SAGE-1D-FP' and for 2D challenges Model 7 'SAGE-ND-FP'. For these algorithms that rely on just one input data type, it is expected that for exhaustive data, performance will be high, while for partial data, the joint SAGE model will outperform these models. These additional algorithms are available as part of the SAGE library.

### Model 4: SAGE-1D-PM, 1-Dimensional PM

Same as Model 2 lines 1-7. Return  $L_s$ .

### Model 5: SAGE-1D-FP, 1-Dimensional Piecewise GP

Same as Model 2 lines 1-6 and 8-10. Return  $L_p$ .

#### Model 6: SAGE-ND-PM, N-Dimensional PM

Same as Model 3 lines 1-6. Return  $L_S$ .

#### Model 7: SAGE-ND-FP, N-Dimensional Piecewise GP

Same as Model 3 lines 1-5 and 7-13. Return  $L_p$ .

## Results

We demonstrate SAGE for 1D and 2D example challenges. For both 1D and 2D, we first investigate performance for 2 edge cases, each with artificial phase maps of 2 phase regions and one artificial target functional property. In the first edge case, structure data is more informative of the change boundary and in the second edge case the functional property data is more informative of the change boundary. These edge cases demonstrate SAGE’s ability to exploit knowledge across both structure and functional property data to improve prediction of both. We then provide an example of SAGE’s multi-data source coregionalization capabilities with a challenge of 2 structure data sources and 2 functional property data sources. This is followed by a real-world application to the (Bi,Sm)(Sc,Fe)O<sub>3</sub> material system.

### 1D Example

The 1D challenges are shown in Figure 3 with the target functional property shown as a black dashed curve and the phase map shown as a dotted red curve that switches between a value of 0 and 1 at  $x = 0.7$ . For the first edge case, structure data (red diamonds) is more informative of the phase boundary, compared to functional property data (black squares). The reverse is true for the second edge case. To compare functional property prediction performance, in Figure 3a and 3b we plot: 1) SAGE-1D’s functional property posterior mean (solid green line) and 95 % confidence interval (shaded green area), 2) an off-the-shelf GP with the changepoint kernel (GP-CP, blue line and shaded area) which uses maximum likelihood estimate (MLE), and 3) a plot of SAGE-1D’s maximum likelihood sample (MLS, magenta line and shaded area) – the MCMC sample with the maximum computed likelihood. For phase boundary prediction comparison, we plot: 1) SAGE-1D’s phase boundary posterior distribution (green inset histogram) and 2) SAGE-1D-PM’s posterior distribution (orange inset histogram).

For the first edge case, SAGE-1D MLS combines structure and functional property knowledge to outperform GP-CP in predicting both functional property and phase boundary. SAGE-1D’s slanted transition at the phase boundary (Figure 1a) indicates a range of potential phase boundary locations between the two structure data points (range is also indicated by the dotted green lines). SAGE-1D and SAGE-1D-PM have similar performance in identifying the phase boundary location, providing similar posteriors (inset). SAGE-1D employs phase boundary uncertainty to better quantify its regression uncertainty as indicated by the wider confidence intervals.

For the second edge case, SAGE-1D MLS and GP-CP have similar regression performance due to the highly informative functional property data. However, SAGE-1D outperforms SAGE-1D-PM in locating the phase boundary, as it exploits functional property data to greatly narrow in on potential locations. A further comparison between SAGE-1D, GP-CP, SAGE-1D-PM, SAGE-1D-FP, and GP classification are presented in Table 1. Knowledge of the changepoint location is limited to the two nearest data points,

either functional property or structure data. As a result, functional property prediction performance is measured outside the range of the two nearest data points.

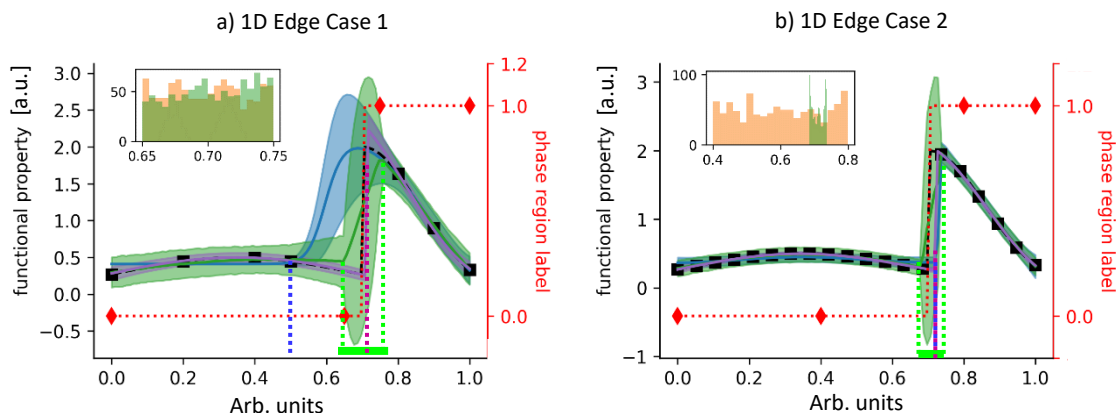


Figure 3. SAGE-1D performance for two edge cases: a) edge case 1 where structure data (red diamonds) is more informative of the phase boundary and b) edge case 2 where functional property data (black squares) is more informative of the phase boundary. Main plots show comparison of: the SAGE-1D posterior mean and 95 % confidence interval (green line and shaded region), and SAGE-1D maximum likelihood sample (magenta line and shaded region), and a GP (blue line and shaded region) with a changepoint kernel and two radial basis function kernels on either side of the changepoint. The ground truth phase map is indicated by a red dotted line and the ground truth functional property function is indicated as a black dashed line. The GP identified changepoint is indicated with a blue dotted line and the range of potential changepoints identified by SAGE-1D is indicated by green dotted lines. The SAGE-1D changepoint posterior is shown as the inset (green histogram) and compared to the SAGE-1D-PM changepoint detection algorithm (orange histogram).

## 2D Example

We observe similar behavior in the 2D demonstration of SAGE-ND as shown in Figure 4. The location of structure data (red squares on phase map plots) and functional property data (red squares on functional property plots) are indicated. For phase map prediction, SAGE-ND is compared to SAGE-ND-PM, SAGE-ND-FP, and GP classification. For functional property prediction, SAGE-ND is compared to SAGE-ND-FP and off-the-shelf GP regression. Performance scores are reported in Table 1. SAGE-ND outperforms the other methods in both phase mapping and functional property prediction for both edge cases. In edge case 2, despite highly informative functional property data, SAGE-ND outperforms off-the-shelf GP regression due to its ability to properly deal with the change in property and change in hyperparameters across the phase boundary.

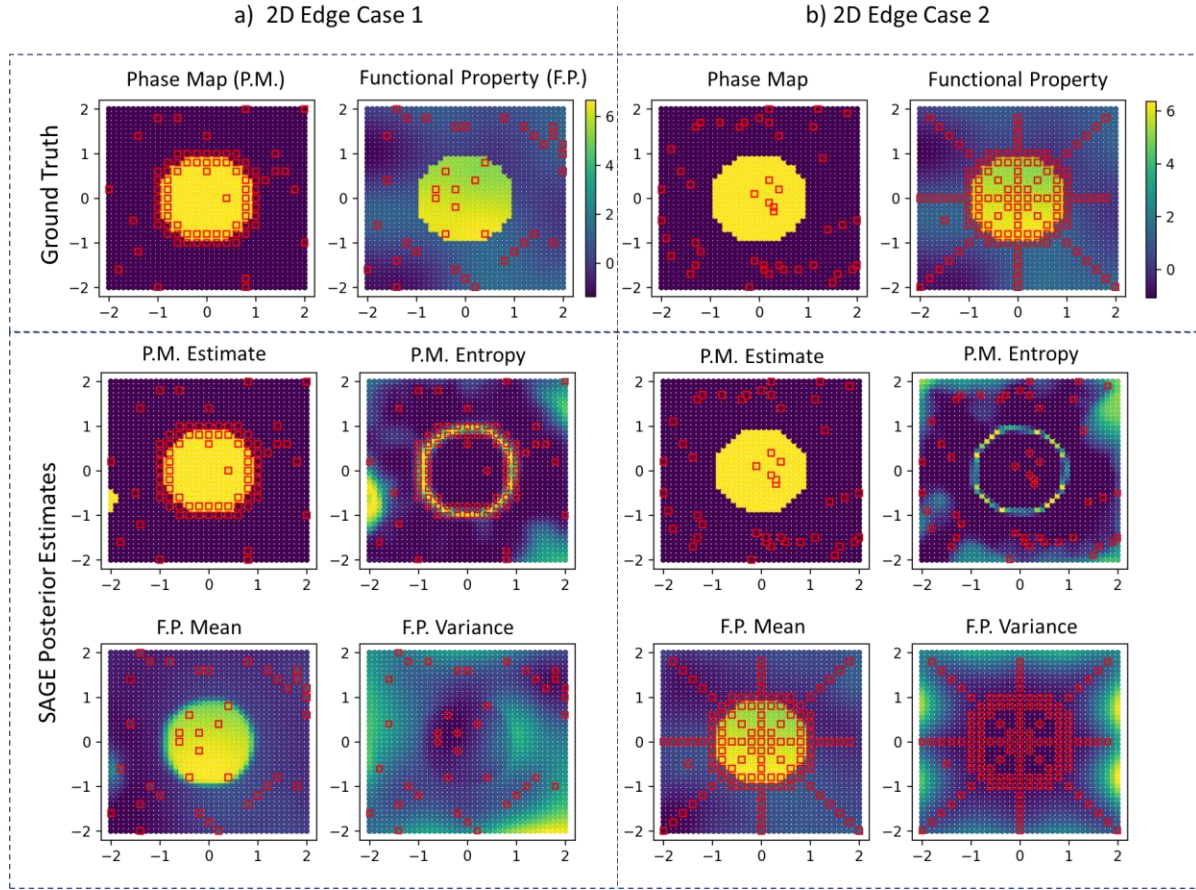


Figure 4. Algorithm demonstration on 2D example for the 2 edge cases: a) edge case 1 where structure data (red squares in phase map plots) is more informative of the phase boundary and b) edge case 2 where functional property data (red squares in functional property plots) is more informative of the phase boundary. The algorithm shows good agreement with the ground truth for both cases.

In Figure 5 we demonstrate the ND algorithm for the 2D case with 2 structure data sources and 2 functional property sources. Here the first structure data source provides more information for the upper part of the phase boundary and the second source provides more information for the lower part of the boundary. SAGE-ND unifies knowledge across all four data sources to obtain good prediction of both phase map and the two functional properties.

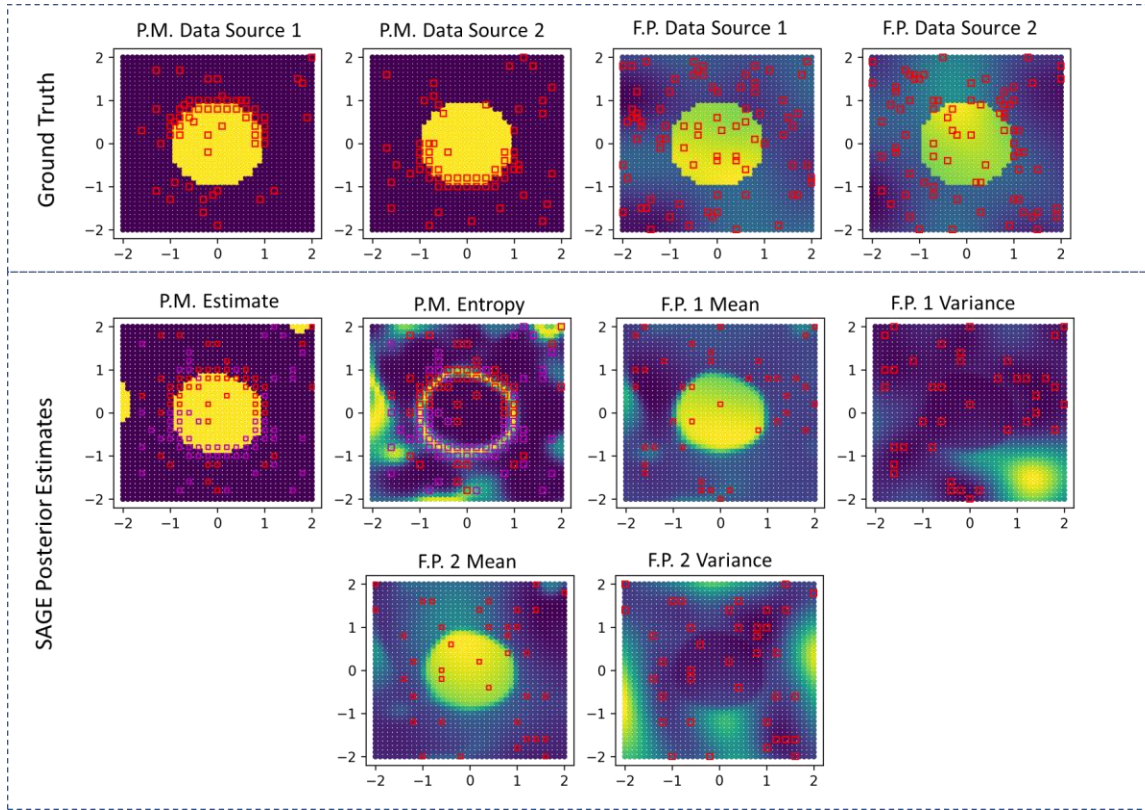


Figure 5. Demonstration of SAGE-ND algorithm for 2 structure data sources and 2 functional property data sources.

### Materials Example: $(\text{Bi},\text{Sm})(\text{Sc},\text{Fe})\text{O}_3$

For the materials challenge demonstration, SAGE-ND is applied to learn a SSPP for a  $(\text{Bi},\text{Sm})(\text{Sc},\text{Fe})\text{O}_3$  composition spread dataset of Raman spectra structure measurements and CEFM drawn from (1, 3) as shown in Figure 6. As structure data is collected primarily to learn the phase map, we present the case where structure data is more informative of the phase boundaries than the functional property data. Phase mapping and CEFM predictions estimates are shown in Figure 6a1 and 6b1 and uncertainties in Figures 6a2 and 6b2 respectively. Given the limited data, SAGE-ND shows good agreement with the ground truth (Figure 1). A comparison of SAGE-ND with SAGE-ND-PM, SAGE-ND-FP, GP classification and GP regression are shown in Table 1 with SAGE-ND outperforming the other algorithms.

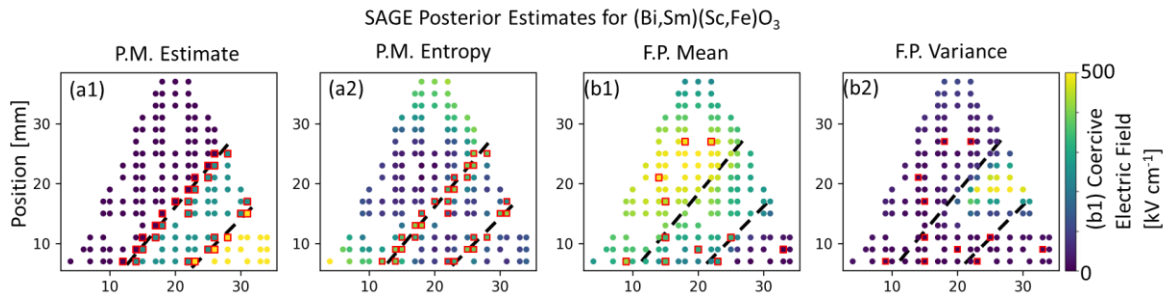


Figure 6. SAGE-ND applied to  $(\text{Bi},\text{Sm})(\text{Sc},\text{Fe})\text{O}_3$  dataset. Figure 1 shows the ground truth. a1) Phase map estimate indicated by color coding with structure data indicated with red squares and phase boundaries indicated by dashed



black lines. a2) entropy-measured uncertainty in the phase map of (a1), b1) CEFM estimate with functional property data indicated with red squares. b2) variance-measured uncertainty for the CEFM estimate.

Performance Table

	Phase Map Performance, Accuracy [arb. units]				
<b>1D Challenges</b>	SAGE-1D (post. mean)	SAGE-1D-PM (post. mean)	SAGE-1D-FP (post. mean)	GP-CP (max likelihood)	GP Classification (max likelihood)
1D Edge Case 1	1.00	1.00	0.97	0.89	1.00
1D Edge Case 2	1.00	0.90	1.00	0.97	0.90
<b>2D Challenges</b>	SAGE-ND (post. mean)	SAGE-ND-PM (post. mean)	SAGE-ND-FP (post. mean)	---	GP Classification (max likelihood)
2D Edge Case 1	0.98	0.97	0.85	---	0.98
2D Edge Case 2	0.98	0.92	0.97	---	0.93
(Bi,Sm)(Sc,Fe)O3	0.99	0.99	0.09	---	0.88
	Functional Property Performance $R^2$ [arb. units]				
<b>1D Challenges</b>	SAGE-1D (post. mean)	---	SAGE-1D-FP (post. mean)	GP-CP (max likelihood)	---
1D Edge Case 1	0.96	---	0.66	-0.06	---
1D Edge Case 2	1.00	---	1.00	0.99	---
<b>2D Challenges</b>	SAGE-ND (post. mean)	---	SAGE-ND-FP (post. mean)	---	GP Regression (max likelihood)
2D Edge Case 1	0.88	---	0.53	---	0.67
2D Edge Case 2	0.89	---	0.87	---	0.62
(Bi,Sm)(Sc,Fe)O3	0.53	---	0.21	---	0.34

Table 1. Performance scores comparing SAGE with alternative algorithms for the 1D and 2D edge cases and the real-world (Bi,Sm)(Sc,Fe)O3 challenge.

## Conclusion

SAGE allows one to combine knowledge of material structure and material property from multiple data sources into one joint SSPR prediction, exploiting shared trends to maximize knowledge of the phase diagram and functional properties. The Bayesian inference methodology allows for appropriate quantification of uncertainty. Furthermore, uncertainty in data can be propagated through the model by sampling the data distributions along with the model parameters or by replacing the piecewise GPs with heteroskedastic GPs. Additionally, correlations between functional properties can also be exploited by replacing the functional property-representing independent piecewise GPs with a coregionalized multi-output GP.

Model output estimates and uncertainties can be employed in active learning-driven recommendation engines or closed-loop autonomous systems, to ensure optimum selection of subsequent experiments. For example, the phase map estimate and uncertainty can guide subsequent structure measurements toward improved phase map knowledge while the paired functional property estimates and uncertainties guide materials optimization. With each experiment increasing knowledge of separate portions of the SSPR, SAGE can play a part in unifying knowledge across a research lab toward the discovery of advanced materials.

## References

1. D. Kan, C. J. Long, C. Steinmetz, S. E. Lofland, I. Takeuchi, Combinatorial search of structural transitions: Systematic investigation of morphotropic phase boundaries in chemically substituted BiFeO<sub>3</sub>. *Journal of Materials Research*. **27**, 2691–2704 (2012).
2. D. Kan, L. Pálová, V. Anbusathaiah, C. J. Cheng, S. Fujino, V. Nagarajan, K. M. Rabe, I. Takeuchi, Universal Behavior and Electric-Field-Induced Structural Transition in Rare-Earth-Substituted BiFeO<sub>3</sub>. *Advanced Functional Materials*. **20**, 1108–1115 (2010).
3. A. G. Kusne, D. Keller, A. Anderson, A. Zaban, I. Takeuchi, High-throughput determination of structural phase diagram and constituent phases using GRENDL. *Nanotechnology*. **26**, 444002 (2015).
4. J. K. Bunn, S. Han, Y. Zhang, Y. Tong, J. Hu, J. R. Hattrick-Simpers, Generalized machine learning technique for automatic phase attribution in time variant high-throughput experimental studies. *Journal of Materials Research*. **30**, 879–889 (2015).
5. J. R. Hattrick-Simpers, J. M. Gregoire, A. G. Kusne, Perspective: Composition–structure–property mapping in high-throughput experiments: Turning data into knowledge. *APL Materials*. **4**, 053211 (2016).
6. D. Chen, Y. Bai, W. Zhao, S. Ament, J. Gregoire, C. Gomes, "Deep Reasoning Networks for Unsupervised Pattern De-mixing with Constraint Reasoning" in *Proceedings of the 37th International Conference on Machine Learning* (PMLR, 2020; <https://proceedings.mlr.press/v119/chen20a.html>), pp. 1500–1509.
7. C. P. Gomes, J. Bai, Y. Xue, J. Björck, B. Rappazzo, S. Ament, R. Bernstein, S. Kong, S. K. Suram, R. B. van Dover, CRYSTAL: a multi-agent AI system for automated mapping of materials' crystal structures. *MRS Communications*. **9**, 600–608 (2019).
8. A. G. Kusne, T. Gao, A. Mehta, L. Ke, M. C. Nguyen, K.-M. Ho, V. Antropov, C.-Z. Wang, M. J. Kramer, C. Long, I. Takeuchi, On-the-fly machine-learning for high-throughput experiments: search for rare-earth-free permanent magnets. *Sci. Rep.* **4** (2014), doi:10.1038/srep06367.
9. A. G. Kusne, H. Yu, C. Wu, H. Zhang, J. Hattrick-Simpers, B. DeCost, S. Sarker, C. Oses, C. Toher, S. Curtarolo, On-the-fly closed-loop materials discovery via Bayesian active learning. *Nature communications*. **11**, 1–11 (2020).
10. R. LeBras, T. Damoulas, J. M. Gregoire, A. Sabharwal, C. P. Gomes, R. B. van Dover, "Constraint reasoning and Kernel clustering for pattern decomposition with scaling" in *Principles and Practice of Constraint Programming–CP 2011* (Springer, 2011), pp. 508–522.
11. C. P. Gomes, J. Bai, Y. Xue, J. Björck, B. Rappazzo, S. Ament, R. Bernstein, S. Kong, S. K. Suram, R. B. van Dover, CRYSTAL: a multi-agent AI system for automated mapping of materials' crystal structures. *MRS Communications*. **9**, 600–608 (2019).
12. Y. Iwasaki, A. G. Kusne, I. Takeuchi, Comparison of dissimilarity measures for cluster analysis of X-ray diffraction data from combinatorial libraries. *npj Computational Materials*. **3**, 1–9 (2017).

13. S. K. Suram, Y. Xue, J. Bai, R. Le Bras, B. Rappazzo, R. Bernstein, J. Bjorck, L. Zhou, R. B. Van Dover, C. P. Gomes, Automated phase mapping with AgileFD and its application to light absorber discovery in the V–Mn–Nb oxide system. *ACS combinatorial science*. **19**, 37–46 (2017).
14. V. Stanev, V. V. Vesselinov, A. G. Kusne, G. Antoszewski, I. Takeuchi, B. S. Alexandrov, Unsupervised phase mapping of X-ray diffraction data by nonnegative matrix factorization integrated with custom clustering. *npj Computational Materials*. **4**, 1–10 (2018).
15. P. M. Maffettone, L. Banko, P. Cui, Y. Lysogorskiy, M. A. Little, D. Olds, A. Ludwig, A. I. Cooper, Crystallography companion agent for high-throughput materials discovery. *Nat Comput Sci*. **1**, 290–297 (2021).
16. Autonomous Experimental Design and Execution | Handbook on Big Data and Machine Learning in the Physical Sciences, (available at [https://www.worldscientific.com/doi/abs/10.1142/9789811204579\\_0013](https://www.worldscientific.com/doi/abs/10.1142/9789811204579_0013)).
17. S. Ament, M. Amsler, D. R. Sutherland, M.-C. Chang, D. Guevarra, A. B. Connolly, J. M. Gregoire, M. O. Thompson, C. P. Gomes, R. B. van Dover, Autonomous materials synthesis via hierarchical active learning of nonequilibrium phase diagrams. *Science Advances* (2021), doi:10.1126/sciadv.abg4930.
18. A. G. Kusne, A. McDannald, Scalable multi-agent lab framework for lab optimization. *Matter* (2023).
19. J. Jing, S. Liu, G. Wang, W. Zhang, C. Sun, Recent advances on image edge detection: A comprehensive review. *Neurocomputing* (2022).
20. C. Park, P. Qiu, J. Carpena-Núñez, R. Rao, M. Susner, B. Maruyama, Sequential adaptive design for jump regression estimation. *IIE Transactions*. **55**, 111–128 (2023).
21. S. Aminikhanghahi, D. J. Cook, A survey of methods for time series change point detection. *Knowl Inf Syst*. **51**, 339–367 (2017).
22. C. Truong, L. Oudre, N. Vayatis, Selective review of offline change point detection methods. *Signal Processing*. **167**, 107299 (2020).
23. Y. Saatçi, R. D. Turner, C. E. Rasmussen, "Gaussian process change point models" in *Proceedings of the 27th International Conference on Machine Learning (ICML-10)* (2010), pp. 927–934.
24. J. Lloyd, D. Duvenaud, R. Grosse, J. Tenenbaum, Z. Ghahramani, "Automatic construction and natural-language description of nonparametric regression models" in *Proceedings of the AAAI Conference on Artificial Intelligence* (2014), vol. 28.
25. M. A. Ziatdinov, Y. Liu, A. N. Morozovska, E. A. Eliseev, X. Zhang, I. Takeuchi, S. V. Kalinin, Hypothesis Learning in Automated Experiment: Application to Combinatorial Materials Libraries. *Advanced Materials*. **34**, 2201345 (2022).
26. A. G. Journel, C. J. Huijbregts, Mining geostatistics. vol. 600 Academic press (1978).



27. M. A. Alvarez, L. Rosasco, N. D. Lawrence, Kernels for vector-valued functions: A review. *arXiv preprint arXiv:1106.6251* (2011).
28. T. Hastie, R. Tibshirani, J. Friedman, T. Hastie, J. Friedman, R. Tibshirani, *The elements of statistical learning* (Springer, 2009; <http://link.springer.com/content/pdf/10.1007/978-0-387-84858-7.pdf>), vol. 2.
29. E. V. Bonilla, K. Chai, C. Williams, Multi-task Gaussian process prediction. *Advances in neural information processing systems*. **20** (2007).
30. C. A. Micchelli, M. Pontil, On learning vector-valued functions. *Neural computation*. **17**, 177–204 (2005).
31. C. Carmeli, E. De Vito, A. Toigo, Vector valued reproducing kernel Hilbert spaces of integrable functions and Mercer theorem. *Analysis and Applications*. **4**, 377–408 (2006).
32. J.-J. Giraldo, M. A. Álvarez, A Fully Natural Gradient Scheme for Improving Inference of the Heterogeneous Multioutput Gaussian Process Model. *IEEE Transactions on Neural Networks and Learning Systems*. **33**, 6429–6442 (2022).
33. E. Wit, E. van den Heuvel, J.-W. Romeijn, ‘All models are wrong...’: an introduction to model uncertainty. *Statistica Neerlandica*. **66**, 217–236 (2012).
34. C. E. Rasmussen, C. K. I. Williams, *Gaussian Processes for Machine Learning* (The MIT Press, Cambridge, Mass, 2005).
35. A. Lui, Gaussian Process Classification Model in various PPLs (2021), (available at <https://luiarthur.github.io/TuringBnpBenchmarks/gpclassify>).